

Chemotherapeutic drug-specific alteration of microvascular blood flow in murine breast cancer as measured by diffuse correlation spectroscopy

GABRIEL RAMIREZ,¹ ASHLEY R. PROCTOR,¹ KI WON JUNG,¹ TONG TONG WU,² SONGFENG HAN,³ RUSSELL R. ADAMS,¹ JINGXUAN REN,¹ DANIEL K. BYUN,¹ KELLEY S. MADDEN,¹ EDWARD B. BROWN,¹ THOMAS H. FOSTER,^{1,3,4} PARISA FARZAM,⁵ TURGUT DURDURAN,^{5,6} AND REGINE CHOE^{1,7,*}

¹Department of Biomedical Engineering, University of Rochester, Rochester, NY 14627, USA

²Department of Biostatistics and Computational Biology, University of Rochester Medical Center, Rochester, NY 14642, USA

³The Institute of Optics, University of Rochester, Rochester, NY 14627, USA

⁴Department of Imaging Sciences, University of Rochester Medical Center, Rochester, NY 14642, USA

⁵ICFO- Institut de Ciències Fotòniques, The Barcelona Institute of Science and Technology, 08860 Castelldefels (Barcelona), Spain

⁶Institució Catalana de Recerca i Estudis Avançats (ICREA), 08015 Barcelona, Spain

⁷Department of Electrical and Computer Engineering, University of Rochester, Rochester, NY 14627, USA

*Regine_Cho@urmc.rochester.edu

Abstract: The non-invasive, *in vivo* measurement of microvascular blood flow has the potential to enhance breast cancer therapy monitoring. Here, longitudinal blood flow of 4T1 murine breast cancer (N=125) under chemotherapy was quantified with diffuse correlation spectroscopy based on layer models. Six different treatment regimens involving doxorubicin, cyclophosphamide, and paclitaxel at clinically relevant doses were investigated. Treatments with cyclophosphamide increased blood flow as early as 3 days after administration, whereas paclitaxel induced a transient blood flow decrease at 1 day after administration. Early blood flow changes correlated strongly with the treatment outcome and distinguished treated from untreated mice individually for effective treatments.

© 2016 Optical Society of America

OCIS codes: (170.3660) Medical optics and biotechnology: Light propagation in tissues; (170.6480) Medical optics and biotechnology: Spectroscopy, Speckle; (290.4210) Scattering: Multiple scattering.

References and links

1. P. Rastogi, S. J. Anderson, H. D. Bear, C. E. Geyer, M. S. Kahlenberg, A. Robidoux, R. G. Margolese, J. L. Hoehn, V. G. Vogel, S. R. Dakhil, D. Tamkus, K. M. King, E. R. Pajon, M. J. Wright, J. Robert, S. Paik, E. P. Mamounas, and N. Wolmark, "Preoperative chemotherapy: updates of National Surgical Adjuvant Breast and Bowel Project Protocols B-18 and B-27," *J. Clin. Onc.* **26**, 778–785 (2008).
2. A. S. Caudle, A. M. Gonzalez-Angulo, K. K. Hunt, P. Liu, L. Pusztai, W. F. Symmans, H. M. Kuerer, E. A. Mittendorf, G. N. Hortobagyi, and F. Meric-Bernstam, "Predictors of tumor progression during neoadjuvant chemotherapy in breast cancer," *J. Clin. Onc.* **28**, 1821–1828 (2010).
3. E. Yeh, P. Slanetz, D. B. Kopans, E. Rafferty, D. Georgian-Smith, L. Moy, E. Halpern, R. Moore, I. Kuter, and A. Taghian, "Prospective comparison of mammography, sonography, and MRI in patients undergoing neoadjuvant chemotherapy for palpable breast cancer," *Am. J. Roentgenol.* **184**, 868–877 (2005).
4. R. Choe and T. Durduran, "Diffuse optical monitoring of the neoadjuvant breast cancer therapy," *IEEE J. Sel. Top. Quantum Electron.* **18**, 1367–1386 (2012).
5. M. Beresford, A. R. Padhani, V. Goh, and A. Makris, "Imaging breast cancer response during neoadjuvant systemic therapy," *Expert Rev. Anticancer Ther.* **5**, 893–905 (2005).
6. L. C. Enfield, A. P. Gibson, J. C. Hebden, and M. Douek, "Optical tomography of breast cancer - monitoring response to primary medical therapy," *Targ. Oncol.* **4**, 219–233 (2009).

7. D. B. Jakubowski, A. E. Cerussi, F. Bevilacqua, N. Shah, D. Hsiang, J. Butler, and B. J. Tromberg, "Monitoring neoadjuvant chemotherapy in breast cancer using quantitative diffuse optical spectroscopy: a case study," *J. Biomed. Opt.* **9**, 230–238 (2004).
8. R. Choe, A. Corlu, K. Lee, T. Durduran, S. D. Konecky, M. Grosicka-Koptyra, S. R. Arridge, B. J. Czerniecki, D. L. Fraker, A. DeMichele, B. Chance, M. A. Rosen, and A. G. Yodh, "Diffuse optical tomography of breast cancer during neoadjuvant chemotherapy: a case study with comparison to MRI," *Med. Phys.* **32**, 1128–1139 (2005).
9. N. Shah, J. Gibbs, D. Wolverton, A. Cerussi, N. Hylton, and B. J. Tromberg, "Combined diffuse optical spectroscopy and contrast-enhanced magnetic resonance imaging for monitoring breast cancer neoadjuvant chemotherapy: a case study," *J. Biomed. Opt.* **10**, 051503 (2005).
10. B. J. Tromberg, A. Cerussi, N. Shah, M. Compton, A. Durkin, D. Hsiang, J. Butler, and R. Mehta, "Imaging in breast cancer: diffuse optics in breast cancer: detecting tumors in pre-menopausal women and monitoring neoadjuvant chemotherapy," *Breast Cancer Res.* **7**, 279–285 (2005).
11. Q. Zhu, S. H. Kurtzman, P. Hegde, S. Tannenbaum, M. Kane, M. Huang, N. G. Chen, B. Jagjivan, and K. Zarfes, "Utilizing optical tomography with ultrasound localization to image heterogeneous hemoglobin distribution in large breast cancers," *Neoplasia* **7**, 263–270 (2005).
12. A. Cerussi, D. Hsiang, N. Shah, R. Mehta, A. Durkin, J. Butler, and B. J. Tromberg, "Predicting response to breast cancer neoadjuvant chemotherapy using diffuse optical spectroscopy," *Proc. Natl. Acad. Sci. U. S. A.* **104**, 4014–4019 (2007).
13. C. Zhou, R. Choe, N. Shah, T. Durduran, G. Yu, A. Durkin, D. Hsiang, R. Mehta, J. Butler, A. Cerussi, B. J. Tromberg, and A. G. Yodh, "Diffuse optical monitoring of blood flow and oxygenation in human breast cancer during early stages of neoadjuvant chemotherapy," *J. Biomed. Opt.* **12**, 051903 (2007).
14. Q. Zhu, S. Tannenbaum, P. Hegde, M. Kane, C. Xu, and S. H. Kurtzman, "Noninvasive monitoring of breast cancer during neoadjuvant chemotherapy using optical tomography with ultrasound localization," *Neoplasia* **10**, 1028–1040 (2008).
15. S. Jiang, B. W. Pogue, C. M. Carpenter, S. P. Poplack, W. A. Wells, C. A. Kogel, J. A. Forero, L. S. Muffly, G. N. Schwartz, K. D. Paulsen, and P. A. Kaufman, "Evaluation of breast tumor response to neoadjuvant chemotherapy with tomographic diffuse optical spectroscopy: Case studies of tumor region-of-interest changes," *Radiology* **252**, 551–560 (2009).
16. H. Soliman, A. Gunasekara, M. Rycroft, J. Zubovits, R. Dent, J. Spayne, M. J. Yaffe, and G. J. Czarnota, "Functional imaging using diffuse optical spectroscopy of neoadjuvant chemotherapy response in women with locally advanced breast cancer," *Clin. Cancer Res.* **16**, 2605–2614 (2010).
17. A. E. Cerussi, V. W. Tanamai, R. S. Mehta, D. Hsiang, J. Butler, and B. J. Tromberg, "Frequent optical imaging during breast cancer neoadjuvant chemotherapy reveals dynamic tumor physiology in an individual patient," *Acad. Radiol.* **17**, 1031–1039 (2010).
18. M. G. Pakalnis, W. A. Wells, M. C. Schwab, H. M. Froehlich, S. Jiang, Z. Li, T. D. Tosteson, S. P. Poplack, P. A. Kaufman, B. W. Pogue, and K. D. Paulsen, "Tumor angiogenesis change estimated by using diffuse optical spectroscopic tomography: Demonstrated correlation in women undergoing neoadjuvant chemotherapy for invasive breast cancer?" *Radiology* **259**, 365–374 (2011).
19. D. Roblyer, S. Ueda, A. Cerussi, W. Tanamai, A. Durkin, R. Mehta, D. Hsiang, J. A. Butler, C. McLaren, W. P. Chen, and B. Tromberg, "Optical imaging of breast cancer oxyhemoglobin flare correlates with neoadjuvant chemotherapy response one day after starting treatment," *Proc. Natl. Acad. Sci. U. S. A.* **108**, 14626–14631 (2011).
20. A. E. Cerussi, V. W. Tanamai, D. Hsiang, J. Butler, R. S. Mehta, and B. J. Tromberg, "Diffuse optical spectroscopic imaging correlates with final pathological response in breast cancer neoadjuvant chemotherapy," *Phil. Trans. R. Soc. A* **369**, 4512–4530 (2011).
21. Y. Santoro, A. Leproux, A. Cerussi, B. Tromberg, and E. Gratton, "Breast cancer spatial heterogeneity in near-infrared spectra and the prediction of neoadjuvant chemotherapy response," *J. Biomed. Opt.* **16**, 097007 (2011).
22. L. C. Enfield, G. Cantanhede, D. Westbroek, M. Douek, A. D. Purushotham, J. C. Hebden, and A. P. Gibson, "Monitoring the response to primary medical therapy for breast cancer using three-dimensional time-resolved optical mammography," *Technol. Cancer Res. Treat.* **10**, 533–547 (2011).
23. Q. Zhu, P. A. DeFusco, A. J. Ricci, E. B. Cronin, P. U. Hegde, M. Kane, B. Tavakoli, Y. Xu, J. Hart, and S. H. Tannenbaum, "Breast cancer: assessing response to neoadjuvant chemotherapy by using US-guided near-infrared tomography," *Radiology* **266**, 433–442 (2012).
24. S. Ueda, D. Roblyer, A. Cerussi, A. Durkin, A. Leproux, Y. Santoro, S. Xu, T. D. O'Sullivan, D. Hsiang, R. Mehta, J. Butler, and B. J. Tromberg, "Baseline tumor oxygen saturation correlates with a pathologic complete response in breast cancer patients undergoing neoadjuvant chemotherapy," *Cancer Res.* **72**, 4318–4328 (2012).
25. H. J. Feldmann, M. Molls, and P. Vaupel, "Blood flow and oxygenation status of human tumors," *Strahlentherapie und Onkologie* **175**, 1–9 (1999).
26. P. Vaupel and M. Hockel, "Blood supply, oxygenation status and metabolic microenvironment of breast cancers: characterization and therapeutic relevance," *Int. J. Oncol.* **17**, 869–879 (2000).
27. M. Hockel and P. Vaupel, "Tumor hypoxia: Definitions and current clinical, biologic, and molecular aspects," *J. Natl. Cancer Inst.* **93**, 266–276 (2001).
28. L. K. Dunnwald, J. R. Gralow, G. K. Ellis, R. B. Livingston, H. M. Linden, J. M. Specht, R. K. Doot, T. J. Lawton, W. E. Barlow, B. F. Kurland, E. K. Schubert, and D. A. Mankoff, "Tumor metabolism and blood flow changes by

- Positron Emission Tomography: Relation to survival in patients treated with neoadjuvant chemotherapy for locally advanced breast cancer," *J. Clin. Oncol.* **26**, 4449–4457 (2008).
29. U. Sunar, H. Quon, T. Durduran, J. Zhang, J. Du, C. Zhou, G. Yu, R. Choe, A. Kilger, R. Lustig, L. Loevner, S. Nioka, B. Chance, and A. G. Yodh, "Noninvasive diffuse optical measurement of blood flow and blood oxygenation for monitoring radiation therapy in patients with head and neck tumors: a pilot study," *J. Biomed. Opt.* **11**, 064021 (2006).
 30. F. Martelli, T. Binzoni, A. Pifferi, L. Spinelli, A. Farina, and A. Torricelli, "There's plenty of light at the bottom: statistics of photon penetration depth in random media," *Sci. Rep.* **6**, 27057 (2016).
 31. L. S. Hansen, J. E. Coggle, J. Wells, and M. W. Charles, "The influence of the hair cycle on the thickness of mouse skin," *Anat. Rec.* **210**, 569–573 (1984).
 32. B. A. Pulaski and S. Ostrand-Rosenberg, "Mouse 4T1 breast tumor model," *Curr. Protoc. Immunol.* **Chapter 20**, Unit 20.2 (2001).
 33. A. S. Betof, C. D. Lascola, D. Weitzel, C. Landon, P. M. Scarbrough, G. R. Devi, G. Palmer, L. W. Jones, and M. W. Dewhirst, "Modulation of murine breast tumor vascularity, hypoxia and chemotherapeutic response by exercise," *J. Natl. Cancer Inst.* **107**, djv040 (2015).
 34. S. Gargiulo, A. Greco, M. Gramanzini, S. Esposito, A. Affuso, A. Brunetti, and G. Vesce, "Mice anesthesia, analgesia, and care, part i: anesthetic considerations in preclinical research," *ILAR J.* **53**, E55–69 (2012).
 35. S. Gargiulo, A. Greco, M. Gramanzini, S. Esposito, A. Affuso, A. Brunetti, and G. Vesce, "Mice anesthesia, analgesia, and care, part ii: anesthetic considerations in preclinical imaging studies," *ILAR J.* **53**, E70–81 (2012).
 36. S. Gargiulo, M. Gramanzini, R. Liuzzi, A. Greco, A. Brunetti, and G. Vesce, "Effects of some anesthetic agents on skin microcirculation evaluated by laser doppler perfusion imaging in mice," *BMC Vet. Res.* **9**, 255 (2013).
 37. M. L. Citron, D. A. Berry, C. Cirincione, C. Hudis, E. P. Winer, W. J. Gradishar, N. E. Davidson, S. Martino, R. Livingston, J. N. Ingle, E. A. Perez, J. Carpenter, D. Hurd, J. F. Holland, B. L. Smith, C. I. Sartor, E. H. Leung, J. Abrams, R. L. Schilsky, H. B. Muss, and L. Norton, "Randomized trial of dose-dense versus conventionally scheduled and sequential versus concurrent combination chemotherapy as postoperative adjuvant treatment of node-positive primary breast cancer: first report of Intergroup Trial C9741/Cancer and Leukemia Group B Trial 9741," *J. Clin. Oncol.* **21**, 1431–1439 (2003).
 38. C. A. Hudis, "Current status and future directions in breast cancer therapy," *Clin. Breast Cancer* **4**, Suppl. 2, S70–S75 (2003).
 39. J. A. Sparano, M. Wang, S. Martino, V. Jones, E. A. Perez, T. Saphner, A. C. Wolff, G. W. J. Sledge, W. C. Wood, and N. E. Davidson, "Weekly paclitaxel in the adjuvant treatment of breast cancer," *N. Engl. J. Med.* **358**, 1663–1671 (2008).
 40. C. F. Thorn, C. Oshiro, S. Marsh, T. Hernandez-Boussard, H. McLeod, T. E. Klein, and R. B. Altman, "Doxorubicin pathways: pharmacodynamics and adverse effects," *Pharmacogenet. Genomics* **21**, 440–446 (2011).
 41. A. Emadi, R. J. Jones, and R. A. Brodsky, "Cyclophosphamide and cancer: golden anniversary," *Nat. Rev. Clin. Oncol.* **6**, 638–647 (2009).
 42. V. A. de Weger, J. H. Beijnen, and J. H. M. Schellens, "Cellular and clinical pharmacology of the taxanes docetaxel and paclitaxel - a review," *Anticancer Drugs* **25**, 488–494 (2014).
 43. S. Reagan-Shaw, M. Nihal, and N. Ahmad, "Dose translation from animal to human studies revisited," *FASEB J.* **22**, 659–661 (2007).
 44. T. Durduran, R. Choe, W. B. Baker, and A. G. Yodh, "Diffuse optics for tissue monitoring and tomography," *Rep. Prog. Phys.* **73**, 076701 (2010).
 45. P. A. Lemieux and D. J. Durian, "Investigating non-gaussian scattering processes by using nth-order intensity correlation functions," *J. Opt. Soc. Am. A* **16**, 1651–1664 (1999).
 46. L. Gagnon, M. Desjardins, J. Jehanne-Lacasse, L. Bherer, and F. Lesage, "Investigation of diffuse correlation spectroscopy in multi-layered media including the human head," *Opt. Express* **16**, 15514–15530 (2008).
 47. A. Kienle, M. S. Patterson, N. Dögnitz, R. Bays, G. Wagnières, and H. van den Bergh, "Noninvasive determination of the optical properties of two-layered turbid media," *Appl. Opt.* **37**, 779–791 (1998).
 48. A. Kienle and T. Glanzmann, "In vivo determination of the optical properties of muscle with time-resolved reflectance using a layered model," *Phys. Med. Biol.* **44**, 2689–2702 (1999).
 49. G. H. Golub and J. H. Welsh, "Calculation of gauss quadrature rules," *Math. Comput.* **23**, 221–230 (1969).
 50. P. Farzam and T. Durduran, "Multidistance diffuse correlation spectroscopy for simultaneous estimation of blood flow index and optical properties," *J. Biomed. Opt.* **20**, 55001 (2015).
 51. K. Vishwanath, H. Yuan, W. T. Barry, M. W. Dewhirst, and N. Ramanujam, "Using optical spectroscopy to longitudinally monitor physiological changes within solid tumors," *Neoplasia* **11**, 889–900 (2009).
 52. S. L. Jacques, "Optical properties of biological tissues: a review," *Phys. Med. Biol.* **58**, R37–R61 (2013).
 53. J. D. Johansson, M. Mireles, J. Morales-Dalmau, P. Farzam, M. Martínez-Lozano, O. Casanovas, and T. Durduran, "Scanning, non-contact, hybrid broadband diffuse optical spectroscopy and diffuse correlation spectroscopy system," *Biomed. Opt. Express* **7**, 481–498 (2016).
 54. J. C. Pinheiro and D. M. Bates, *Mixed-Effects Models in S and S-PLUS* (Springer, 2000).
 55. G. M. Fitzmaurice, N. M. Laird, and J. H. Ware, *Applied Longitudinal Analysis* (John Wiley & Sons, Inc. 1962).
 56. G. Cocconi, B. Di Blasio, G. Alberti, G. Bisagni, E. Botti, and G. Peracchia, "Problems in evaluating response of primary breast cancer to systemic therapy," *Breast Cancer Res. Treat.* **4**, 309–313 (1984).

57. M. C. Segel, D. D. Paulus, and G. N. Hortobagyi, "Advanced primary breast cancer: assessment at mammography of response to induction chemotherapy," *Radiology* **169**, 49–54 (1988).
58. S. J. Vinnicombe, A. D. MacVica, R. L. Guy, J. P. Sloane, T. J. Powles, G. Knee, and J. E. Husband, "Primary breast cancer: mammographic changes after neoadjuvant chemotherapy, with pathologic correlation," *Radiology* **198**, 333–340 (1996).
59. J. L. Evelhoch, R. J. Gillies, G. S. Karczmar, J. A. Koutcher, R. J. Maxwell, O. Nalcioglu, N. Raghunand, S. M. Ronen, B. D. Ross, and H. M. Swartz, "Applications of magnetic resonance in model systems: cancer therapeutics," *Neoplasia* **2**, 152–165 (2000).
60. K. Vishwanath, D. Klein, K. Chang, T. Schroeder, M. W. Dewhirst, and N. Ramanujam, "Quantitative optical spectroscopy can identify long-term local tumor control in irradiated murine head and neck xenografts," *J. Biomed. Opt.* **14**, 054051 (2009).
61. G. Yu, T. Durduran, C. Zhou, H. W. Wang, M. E. Putt, M. Saunders, C. M. Sehgal, E. Glatstein, A. G. Yodh, and T. M. Busch, "Noninvasive monitoring of murine tumor blood flow during and after photodynamic therapy provides early assessment of therapeutic efficacy," *Clin. Cancer Res.* **11**, 3543–3552 (2005).
62. U. Sunar, S. Makonnen, C. Zhou, T. Durduran, G. Yu, H. W. Wang, W. M. F. Lee, and A. G. Yodh, "Hemodynamic responses to antivasular therapy and ionizing radiation assessed by diffuse optical spectroscopies," *Opt. Express* **15**, 15507–15516 (2007).
63. J. E. Talmadge, R. K. Singh, I. J. Fidler, and A. Raz, "Murine models to evaluate novel and conventional therapeutic strategies for cancer," *Am. J. Pathol.* **170**, 793–804 (2007).
64. Y. Shang and G. Yu, "A Nth-order linear algorithm for extracting diffuse correlation spectroscopy blood flow indices in heterogeneous tissues," *Appl. Phys. Lett.* **105**, 133702 (2014).
65. T. Stylianopoulos, J. D. Martin, V. P. Chauhan, S. R. Jain, B. Diop-Frimpong, N. Bardeesy, B. L. Smith, C. R. Ferrone, F. J. Hornicek, Y. Boucher, L. L. Munn, and R. K. Jain, "Causes, consequences, and remedies for growth-induced solid stress in murine and human tumors," *Proc. Natl. Acad. Sci. USA* **109**, 15101–15108 (2012).
66. R. K. Jain, J. D. Martin, and T. Stylianopoulos, "The role of mechanical forces in tumor growth and therapy," *Annu. Rev. Biomed. Eng.* **16**, 321–346 (2014).
67. R. K. Jain, "Normalization of tumor vasculature: an emerging concept in antiangiogenic therapy," *Science* **307**, 58–62 (2005).
68. M. Mark, R. Walter, D. O. Meredith, and W. H. Reinhart, "Commercial taxane formulations induce stomatocytosis and increase blood viscosity," *Br. J. Pharmacol.* **134**, 1207–1214 (2001).
69. E. Pasquier, M. Carré, B. Pourroy, L. Camoin, O. Rebaï, C. Briand, and D. Braguer, "Antiangiogenic activity of paclitaxel is associated with its cytostatic effect, mediated by the initiation but not completion of a mitochondrial apoptotic signaling pathway," *Mol. Cancer Ther.* **3**, 1301–1310 (2004).
70. J. Alexandre, Y. Hu, W. Lu, H. Pelicano, and P. Huang, "Novel action of paclitaxel against cancer cells: bystander effect mediated by reactive oxygen species," *Cancer Res.* **67**, 3512–3517 (2007).
71. T. Durduran (Personal communication, August 11, 2016).
72. S. Han, J. Johansson, M. Mireles, A. R. Proctor, M. D. Hoffman, J. B. Vella, D. S. W. Benoit, T. Durduran, and R. Choe, "Non-contact scanning diffuse correlation tomography system for three-dimensional blood flow imaging in a murine bone graft model," *Biomed. Opt. Express* **6**, 2695–2712 (2015).
73. S. Han, A. R. Proctor, J. B. Vella, D. S. W. Benoit, and R. Choe, "Non-invasive diffuse correlation tomography reveals spatial and temporal blood flow differences in murine bone grafting approaches," *Biomed. Opt. Express* **7**, 3262–3279 (2016).

1. Introduction

Patients with locally advanced breast cancer generally receive neoadjuvant chemotherapy (NAC) to shrink breast tumors prior to surgical removal. However, up to 20% of these patients do not respond to this therapy [1, 2]. Due to the lack of reliable methods to monitor and predict therapeutic efficacy at an early stage in the course of treatment, these non-responders suffer from unnecessary side effects of ineffective treatments and may lose opportunities for alternative treatments. Current NAC response estimation methods such as clinical palpation, mammography, and ultrasonography are based on morphological changes and are inaccurate for prediction of therapeutic efficacy [3, 4]. Several research studies employing positron emission tomography (PET) and/or dynamic contrast enhanced magnetic resonance imaging (DCE-MRI) have demonstrated that metabolic and physiological changes, as early as 24 hours after the initial NAC cycle, correlate well with pathological or clinical responses [5]. However, it is difficult to employ PET and DCE-MRI as imaging modalities for frequent longitudinal monitoring due to the high cost and the requirement of contrast agent injection.

Diffuse optical methods are non-invasive techniques suitable for frequent longitudinal

monitoring of functional parameters because they do not use ionizing radiation or contrast agent injection, and are inexpensive [4]. In particular, diffuse optical spectroscopy and tomography measure total hemoglobin concentration, tissue blood oxygenation, water, lipid concentrations and tissue scattering. Diffuse correlation spectroscopy and tomography measure microvascular blood flow information.

Several studies on human subjects have demonstrated that diffuse optical spectroscopy and tomography are sensitive to changes induced by breast cancer therapies and have the potential to predict therapeutic efficacy [4, 6–24]. In particular, the decrease of breast cancer total hemoglobin concentration in good responders was consistently observed in most studies at least one month after the initial administration of therapeutic treatments [4], in line with changes in angiogenesis [18]. In terms of early responses, Roblyer *et al.* [19] noted a significant transient increase (flare) of oxygenated hemoglobin concentration in responders one day after the initial chemotherapy administration regardless of the type of therapy (e.g., cytotoxic with or without bevacizumab or trastuzumab). This flare was speculated to be due to perfusion changes by an acute inflammatory response induced by cell damage and death, but was not confirmed since the authors did not have direct access to blood flow information.

Blood flow affects the sensitivity of cancer cells to various therapies and is directly related to the systemic delivery of therapeutic drugs [25–27]. In addition, blood flow changes in breast cancer patients undergoing NAC, measured with ^{15}O -water PET, were shown to predict disease-free-survival and overall-survival in human subjects [28]. A few clinical case studies suggested that blood flow flare quantified with diffuse correlation spectroscopy (DCS) may be related to better outcome for breast cancer undergoing chemotherapy [4, 13] and head and neck cancer undergoing radiation therapy [29].

Since these DCS studies were based on a small number of subjects ($N < 10$), it is still unclear whether the blood flow flare is a universal indicator of favorable response to different types of cancer therapies. Furthermore, the earliest time point that blood flow changes can be utilized to reliably predict the treatment efficacy has not been identified. A preclinical model can provide an alternative method to systematically investigate the effects of different chemotherapeutic drugs on hemodynamic parameters at a faster pace than clinical trials. Here, we have investigated the longitudinal effect of commonly used NAC drugs on blood flow quantified with diffuse correlation spectroscopy using 125 murine breast tumors. In particular, six treatment regimens were carefully designed to investigate the individual or combinatorial effect of doxorubicin, cyclophosphamide, and paclitaxel, based on the clinically equivalent dose and the median lethal dose for mice. To improve the accuracy of blood flow, a layer-model based multi-distance DCS data analysis algorithm was developed to account for scab formation in the 4T1 tumors. After quantification of tumor blood flow, a linear mixed effects model was utilized for statistical analysis of longitudinal data. In effective treatments, early changes in relative tumor blood flow correlated well with the treatment outcome (i.e., tumor size changes). Furthermore, the feasibility of utilizing blood flow changes at early time points to predict individual response to cancer treatments was demonstrated.

2. Methods

2.1. Diffuse correlation spectroscopy instrument

This study utilized a diffuse correlation spectroscopy (DCS) system with a 785 nm long coherence laser (DL785-120-SO, CrystaLaser, Reno, NV), and a detection unit consisting of a four-channel photon-counting avalanche photodetector (SPCM-AQ4C, Excelitas, Waltham, MA) and a four-channel hardware correlator board (Flex03OEM, Correlator.com, Bridgewater, NJ). The correlator board calculates the normalized intensity temporal autocorrelation function $g_2(\mathbf{r}, \tau) = \langle I(\mathbf{r}, t)I(\mathbf{r}, t + \tau) \rangle / \langle I(\mathbf{r}, t) \rangle^2$ where $I(\mathbf{r}, t)$ is the intensity measured with the detector at position \mathbf{r} and time t , τ is the correlation delay time, and $\langle \rangle$ denotes ensemble average.

A custom-made probe (Fiberoptic Systems, Inc., Simi Valley, CA) contained one multi-mode fiber with 200 μm diameter for the source and four single-mode fibers with 5.6 μm mode field diameter for detectors as shown in Fig. 1. Source-detector separations were 2.55, 2.89, 3.25 and 3.94 mm. The mean maximum penetration depths reached by photons migrating in homogeneous medium of $\mu_a = 0.1 \text{ cm}^{-1}$ and $\mu'_s = 10 \text{ cm}^{-1}$ at these separations are 1.2 - 3.2 mm [30]. These depths are well above the thickness of murine epidermis and dermis, which is 10 μm and 250 μm respectively [31]. The probe was connected to a micromanipulator with fine control over vertical movement, which, in turn, was connected to a post mounted on a linear translational stage, enabling horizontal movement.

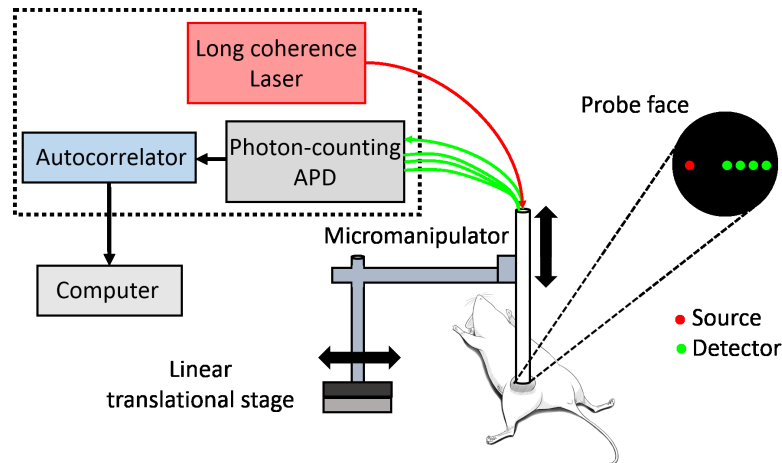


Fig. 1. Diagram of diffuse correlation spectroscopy and probe placement on a murine breast tumor in the mammary fat-pad. After the mouse was anesthetized with isoflurane, a custom-made probe was placed on the center of the tumor. A micromanipulator and a linear translational stage attached to the probe were utilized to enable placement of the probe on the same location within the tumor each day. A multi-mode optical fiber in the probe delivered near-infrared light from a 785 nm long coherence laser to the tumor surface. Light signals detected at four single-mode optical fibers placed 2.55, 2.89, 3.25 and 3.94 mm away from the source fiber were relayed to photon-counting avalanche photodiodes (APDs). Normalized temporal intensity autocorrelation functions of the detected light were calculated by an autocorrelator board and passed onto the computer.

2.2. Animal model and DCS measurement protocol

All experimental protocols were approved by the University Committee on Animal Resources (UCAR) of the University of Rochester. 5-6 week old female BALB/cByJ mice (Jackson Laboratory, Bar Harbor, Maine) were used for this study. Each mouse was injected with the 4T1 murine breast cancer cell line in a mammary fat-pad at a concentration of 1×10^5 cells/100 μL . The 4T1 cancer cell line is syngeneic, originally derived from the corresponding immunocompetent mouse strain (BALB/c) [32, 33].

After the tumor cells were inoculated, the tumor size was measured with a digital caliper on a daily basis. The size was then assessed in terms of area based on the formula $\pi ab/4$, where a and b were the horizontal width and the vertical length, respectively. When the tumor area reached approximately 30 - 35 mm^2 (i.e., an effective diameter of 6 - 7 mm), the *in vivo* mouse experiment using a DCS instrument was initiated. On the first day (Day 0) of the experiment the baseline DCS signals were measured at the center of the tumor under inhalation anesthesia with isoflurane. Isoflurane was chosen mainly for its minimal interference with microcirculation, in

addition to its fast anesthetic effect and reliability [34–36]. Each DCS measurement comprised of the acquisition of thirty sequential autocorrelation functions with 2 second integration time. Measurements were repeated three times at the same location by lifting the probe up and down on the tissue.

After the baseline measurements, intraperitoneal injection of a chemotherapeutic drug dissolved in 200 μL of solvent was given to the mice belonging to the treatment group. For the control group, 200 μL of solvent without any drug was administered. Dulbecco's Phosphate Buffered Saline (DPBS, 21-030-CV, Corning Cellgro) was utilized as the main solvent to maintain physiological pH, unless the drug was water-insoluble. DCS measurements were repeated on days 1, 3, 5, 7, 9, and 11 after the injection.

2.3. Design of clinically motivated chemotherapeutic treatment regimens

In Table 1, chemotherapeutic drug, dose and number of mice for each treatment group are described. Tumor size and DCS measurements were performed in six different treatment groups and one control group. The treatment groups were designed to reflect the dosage of the clinically utilized chemotherapeutic agents. In particular, three chemotherapeutic drugs used for neoadjuvant breast cancer chemotherapy in the clinic were chosen: doxorubicin (brand name: Adriamycin), cyclophosphamide, and paclitaxel (brand name: Taxol). The current study design was based on one of commonly utilized treatment schema for neoadjuvant chemotherapy: 4 cycles of doxorubicin (60 mg/m^2) and cyclophosphamide (600 mg/m^2) followed by 4 cycles of taxane (either paclitaxel 175 mg/m^2 or docetaxel 100 mg/m^2) [37–39]. Initially, experiments involving the control group and treatment group 3 and 4 were performed with more than 25 mice per group. Based on the data from these experiments, the minimum number of mice to detect equivalent changes at day 7 was determined to be 10 mice per group. When the study design was expanded to include other treatment groups, 10 mice per group were utilized to explore the responses to different treatments while conserving resources. Treatment group 5 started out with 10 mice, but two mice were excluded due to unusually slow tumor growth from abnormal tumor cell injection.

Table 1. Treatment and control group information. Treatment group received 200 μL solution of chemotherapeutic drug of the listed dose, whereas control group received 200 μL of DPBS. NA: Not applicable.

Group	Drug	Dose (mg/kg)	# of mice
Treatment group 1	doxorubicin	10	10
Treatment group 2	cyclophosphamide	100	10
Treatment group 3	doxorubicin & cyclophosphamide	10	25
Treatment group 4	cyclophosphamide	100	26
Treatment group 5	paclitaxel	40	8
Treatment group 6	paclitaxel	60	10
Control	NA	NA	36
TOTAL			125

Doxorubicin is an anthracycline antibiotic with two proposed mechanisms of action: (1) intercalation into DNA and disruption of DNA repair by topoisomerase II, and (2) generation of free radicals that damage cellular membranes, proteins, and DNA [40]. Cyclophosphamide is a cytotoxic anticancer agent that works by interfering with DNA replication [41]. Clinically, these two drugs are typically administered concurrently to breast cancer patients undergoing chemotherapy as a part of an Adriamycin-Cyclophosphamide (AC) cocktail [38]. Paclitaxel is a taxane that facilitates the formation of stable tubulin bundles by binding to microtubules and

disrupting their assembly and disassembly [42]. The cell cycle is halted between metaphase and anaphase and, thus, cell proliferation is inhibited.

To translate the clinical dose to animals, the body surface area normalization method is required, instead of simple conversion based on body weight [43]. For mice, the equivalent doses accounting for this normalization are 20 mg/kg, 200 mg/kg and 58 mg/kg for doxorubicin, cyclophosphamide and paclitaxel, respectively. However, the LD₅₀ (median lethal dose), the amount needed to kill 50% of the test population, for intraperitoneal injection in mice is 11.16 mg/kg, 250 mg/kg and 120 mg/kg for doxorubicin, cyclophosphamide, and paclitaxel, respectively. Since the intraperitoneal doxorubicin LD₅₀ for mice is low, the drug administration scheme involving doxorubicin was scaled to half of the equivalent dose (i.e., 10 mg/kg). For treatment group 1 and 3, although the doxorubicin dose was near LD₅₀, most mice survived up to 2 weeks after drug administration.

Since cyclophosphamide is water soluble, it was dissolved directly in DPBS. Doxorubicin was dissolved in dimethyl sulfoxide (DMSO) first, then mixed with DPBS. DMSO concentration was less than 5% of the solution. For paclitaxel, since it is water insoluble, the powder was dissolved in anhydrous ethanol first, then polyethoxylated castor oil (trade name: Kolliphor EL) was added. Kolliphor EL acts as an emulsifier to improve delivery of paclitaxel. Finally, DPBS was added. The ratio among anhydrous ethanol:Kolliphor EL:DPBS was 1:1:8.

Treatment group 1 and 2 were designed to investigate the effect of doxorubicin and cyclophosphamide as a single agent, whereas group 3 was designed for the effect of combining two drugs, simulating the cocktail strategy commonly employed in the clinic. Note that the ratio between two drugs were kept the same as that of the clinical dose (doxorubicin:cyclophosphamide = 1:10) [37, 39]. Treatment group 4 was for investigating the effect of increasing cyclophosphamide to the clinically equivalent dose for the mouse. The effect of paclitaxel was explored through treatment group 5 and 6. Group 6 received 60 mg/kg of paclitaxel, which was the clinically equivalent dose for the mouse, whereas group 5 received 40 mg/kg of paclitaxel, much less than the equivalent dose.

3. Data analysis

3.1. Analytic solution for a homogeneous semi-infinite medium

The correlation diffusion equation [44] describes the propagation of the electric field temporal autocorrelation function, $G_1(\mathbf{r}, \tau)$ where \mathbf{r} is the position and τ is the correlation delay time. The analytic solution of the correlation diffusion equation for a homogeneous medium in semi-infinite geometry (denoted as one-layer medium hereafter) at the tissue boundary (i.e., axial position $z = 0$) is

$$G_1(\rho, \tau) = \frac{vS_0}{4\pi D} \left[\frac{\exp(-K(\tau)r_1)}{r_1} - \frac{\exp(-K(\tau)r_2)}{r_2} \right] \quad (1)$$

$$\text{where } K(\tau) = [(v/D)(\mu_a + 2\tau\mu'_s\kappa_0^2 BFI)]^{1/2} \quad (2)$$

Here ρ is the source-detector separation, v is the speed of light in the medium, S_0 is the light source term, $D \cong v/(3\mu'_s)$ is the light diffusion coefficient, μ'_s is the reduced scattering coefficient, μ_a is the absorption coefficient, $r_1 = [z_0^2 + \rho^2]^{1/2}$, $r_2 = [(z_0 + 2z_b)^2 + \rho^2]^{1/2}$, $z_0 = 1/\mu'_s$ is the transport mean-free path, $z_b = 2(1 + R_{eff})/(3\mu'_s(1 - R_{eff}))$ satisfies the extrapolated zero boundary condition and $R_{eff} \cong -1.440n^{-2} + 0.710n^{-1} + 0.668 + 0.0636n$ is the effective reflection coefficient, and n is the refractive index ratio between the tissue and the air, κ_0 is the light wavevector in the medium, and BFI is the blood flow index based on the Brownian model.

In practice, the normalized intensity temporal autocorrelation function g_2 is measured instead of G_1 [44]. The Siegert relation [45], $g_2(\mathbf{r}, \tau) = 1 + \beta|g_1(\mathbf{r}, \tau)|^2$, links these two functions.

(Note that $g_1(\mathbf{r}, \tau) = G_1(\mathbf{r}, \tau)/G_1(\mathbf{r}, 0)$ is the normalized electric field temporal autocorrelation function.) In this relation β is a parameter that depends on the system characteristics such as source coherence, detection optics, and external factors (e.g., ambient light).

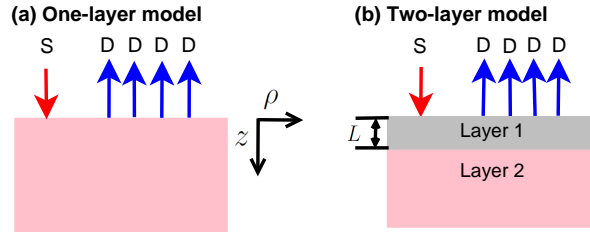


Fig. 2. Schematic of (a) a homogeneous semi-infinite medium (one-layer model), and (b) a semi-infinite two-layer medium (two-layer model) with a source (S) and four detectors (D) on the tissue surface ($z = 0$).

3.2. Analytic solution for a semi-infinite two-layer medium

For a turbid medium consisting of two layers, where the first layer has thickness L and the second layer is semi-infinite, the analytical solution for $z = 0$, as provided by Gagnon *et al.* [46] and derived by Kienle *et al.* [47,48], is

$$G_1^{(1)}(\rho, \tau) = \frac{S_0}{2\pi} \int_0^\infty \tilde{G}_1^{(1)}(s, \tau) s J_0(s\rho) ds, \quad (3)$$

where $^{(1)}$ signifies the first layer, $\tilde{G}_1^{(1)}$ is the inverse Fourier transform of $G_1^{(1)}$, s is the radial frequency, and J_0 is the Bessel function of zeroth order.

$$\tilde{G}_1^{(1)}(s, \tau) = \frac{\frac{v \sinh[A_1(z_b + z_0)]}{D_1 A_1} \frac{D_1 A_1 \cosh(A_1 L) + D_2 A_2 \sinh(A_1 L)}{D_1 A_1 \cosh[A_1(L + z_b)] + D_2 A_2 \sinh[(A_1(L + z_b))]} - \frac{v \sinh(A_1 z_0)}{D_1 A_1}, \quad (4)$$

where, $A_j^2 = (D_j s^2 + v\mu_{a,j} + 2v\tau\mu'_{s,j}\kappa_0^2 BFI_j)/D_j$ for layer j . Here, $\mu_{a,j}$ are the absorption coefficients, $\mu'_{s,j}$ are the reduced scattering coefficients, $D_j \cong v/(3\mu'_{s,j})$ is the light diffusion coefficient, BFI_j is the blood flow index for the first layer ($j = 1$) and for the second layer ($j = 2$). To prevent the introduction of significant computational errors [48], the hyperbolic functions are typically converted to their corresponding exponential forms. Finally, the Hankel Transform in Eq. (3) is then numerically solved using a Gauss-Laguerre quadrature [49].

3.3. Multi-distance, hybrid algorithm based on layer models to extract blood flow index

During the monitoring period, we observed frequent formation of a scab on the surface of the 4T1 tumor, especially towards the later part of the monitoring period. This was in line with the characteristics of 4T1 tumors: $\sim 70\%$ of tumors display ulcerations of the skin [32]. The presence of the scab affects the measured g_2 such that the analytic solution for a homogeneous semi-infinite medium (i.e., one-layer model) does not fit satisfactorily, due to significantly reduced blood flow within the scab. Figure 3 shows an example of such cases: satisfactory fit was achieved with the one-layer model for measured g_2 at day 0 without scab (Fig. 3(a)) whereas the fit was unsatisfactory for measured g_2 at day 11 with a scab (Fig. 3(b)). On the other hand, the two-layer analytic solution [46] assigning the scab as the top layer (layer 1) and the tumor as the bottom layer (layer 2) resulted in a good fit for g_2 at day 11 (Fig. 3(c)). Therefore, a hybrid

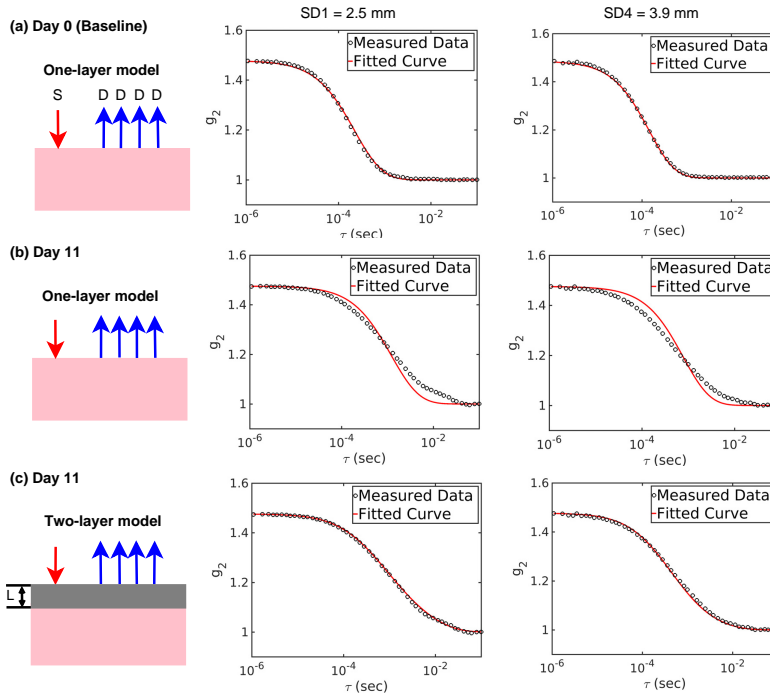


Fig. 3. Example of *in vivo* DCS data from a mouse tumor in the control group at different time points and varying quality of fits. Black circle is the measured data and the red line is the fitted curve from multi-distance fitting of the analytic solution to different layer models. Only data from source-detector separations 2.5 and 3.9 mm are shown for clarity. The quality of one-layer model fit is good for (a) DCS measurements at day 0 ($BFI = 1.38 \times 10^{-8} \text{ cm}^2/\text{s}$), but poor for (b) DCS measurements at day 11 ($BFI = 2.03 \times 10^{-9} \text{ cm}^2/\text{s}$). Two-layer model provides a good fit for (c) DCS measurements at day 11 ($BFI_1 = 3.34 \times 10^{-10} \text{ cm}^2/\text{s}$, $BFI_2 = 9.21 \times 10^{-9} \text{ cm}^2/\text{s}$ with $L = 0.17 \text{ cm}$). S: source, D: detector.

algorithm was developed to accurately quantify the blood flow index of the tumor by separating the signal contribution from scabs using one- or two-layer models. The complete algorithm is shown in Fig. 4 and details of the algorithm are described in the following.

To further improve the fitting fidelity, a multi-distance fitting technique for DCS [50] was adapted for the one-layer and the two-layer solution fit. Typically, blood flow index is quantified from a measurement from a single source-detector pair. However, Farzam *et al.* [50] demonstrated that an objective function combining measurements from multiple source-detector pairs (i.e., multi-distance measurements) is superior to that with a single source-detector pair in terms of retrieval of stable BFI values. This multi-distance approach improves the convergence of the algorithm by confining the minimum of the objective function to a smaller area in parameter space (i.e., less parameter crosstalk). The multi-distance objective function [50] was defined as

$$\chi^2 = \sum_i^{N_{sd}} \sum_j^{N_\tau} \|g_{2,m}(\mathbf{r}_i, \tau_j) - (1 + \beta_i |g_{1,c}(\mathbf{r}_i, \tau_j)|^2)\|, \quad (5)$$

where N_{sd} is the total number of source-detector separations, N_τ is the total number of τ values, $g_{2,m}$ is the measured g_2 and $g_{1,c}$ is the calculated g_1 based on a layer model.

For the two-layer case, there were eleven unknowns for our measurements: $\mu_{a,1}$, $\mu_{a,2}$, $\mu'_{s,1}$,

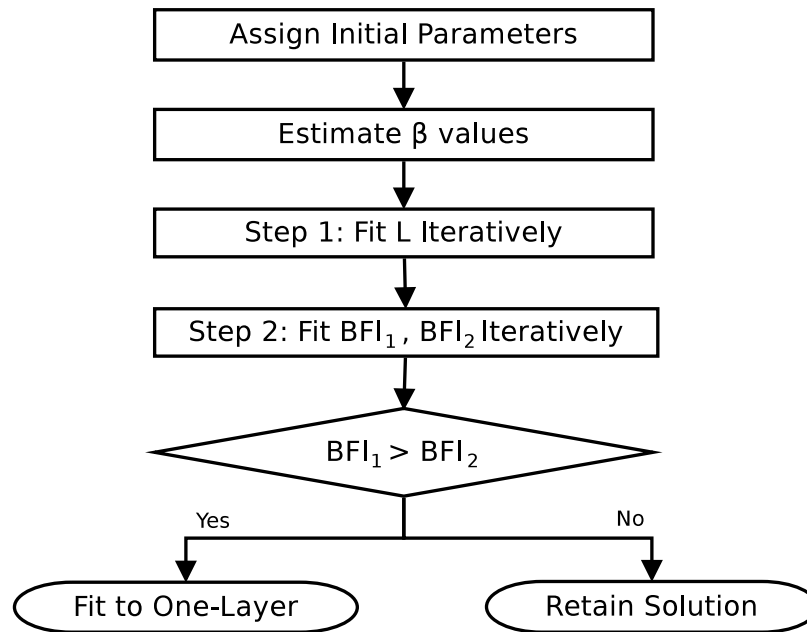


Fig. 4. Flow chart for hybrid algorithm based on layer models to separate the effect of scab on tumor blood flow quantification.

$\mu'_{s,2}$, BFI_1 , BFI_2 , L , and one β for each detector. β for each detector was estimated from the experimental data at short τ ($\sim 10^{-7}$ sec) based on the Siegert relation. To reduce the number of parameters, the optical properties were assumed to be $\mu_{a,1} = \mu_{a,2} = 0.10 \text{ cm}^{-1}$, $\mu'_{s,1} = \mu'_{s,2} = 8.0 \text{ cm}^{-1}$ [51–53]. (Note that these optical properties do not alter the relative blood flow trend as long as consistent values are used. See Section 5.3 for further discussion.) Even with this reduction of unknown parameters, the simultaneous retrieval of three parameters was not stable against the variation of initial guesses. This sensitivity to initial guesses for fitting the layer thickness and optical properties was observed in the multi-layer model [47]. To overcome this instability, a two-step fitting process has been developed (Fig. 4). First, L was fitted under the assumption that BFI_1 and BFI_2 were $10^{-10} \text{ cm}^2/\text{s}$, and $10^{-8} \text{ cm}^2/\text{s}$, respectively. BFI of $10^{-8} \text{ cm}^2/\text{s}$ is the typical order of magnitude found from DCS measurements on *in vivo* tissues without scabs, whereas $10^{-10} \text{ cm}^2/\text{s}$ corresponds to the average BFI from large scabs ($> 3 \text{ mm}$ thick) using the semi-infinite analytical solution at source-detector separation of 2.55 mm. The constrained Nelder-Mead simplex optimization method, which is an iterative fitting method, was utilized for fitting L using MATLAB. The BFI_1 and BFI_2 were then fitted by fixing the L from the previous step using the same optimization method. The stopping criterion was set such that the difference between the current and the previous χ^2 is less than 10^{-6} . Note that thirty consecutively acquired g_2 curves were averaged and used as $g_{2,m}$ to minimize noise in the signal.

In many cases, the fitted BFI_1 was smaller than BFI_2 as expected from the scab. For cases with the larger fitted BFI_1 compared to BFI_2 , the data could be successfully fitted with a one-layer solution. These cases usually corresponded to the data from murine tumors with no or little scabs, measured at earlier monitoring time points (most notably at the baseline point). Thus, we utilized this behavior (i.e., $BFI_1 > BFI_2$) as a condition to determine whether to change the analysis to use a one-layer model (i.e., semi-infinite solution) or retain BFI_2 from the two-layer model as tumor blood flow.

For each mouse at each day of measurement, the BFI (one-layer model) or BFI_2 (two-layer model) values from the three repeated measurements were averaged. Then, the relative blood flow (rBF) of each mouse was computed by normalizing blood flow index with respect to the first time point (i.e., Day 0): for example, $rBF(t) = BFI(t)/BFI(t_{Day0})$ for the one-layer model, where t is the time point. The relative tumor area (rTA) was also calculated in the same fashion: $rTA(t) = TA(t)/TA(t_{Day0})$.

3.4. Statistical analysis

Statistical analysis of data was performed using MATLAB and R. First, student's t-test for data with a normal distribution or Wilcoxon rank-sum test for data with a non-normal distribution was utilized to compare rTA or rBF at each time point between the control and the treatment group, as a quick preliminary assessment. In particular, this method was useful in identifying potential candidates for time points that showed promise for early detection of efficacy. Although this simple method can be beneficial for a quick look at the trend, it does not take into account the longitudinal nature of our dataset.

Therefore, a linear mixed effects model [54] was employed to determine if the longitudinal responses from different treatment groups were statistically different from the control group. The mean response is modeled as a combination of population characteristics common to all individuals (fixed effects) and subject-specific effects unique to a particular individual (random effects) in a mixed effects model [55].

For our case, the expression of the response variable based on the linear mixed effects model was described as

$$Y_{i,j,m} = \beta_{0,0} + \beta_{1,0} \times t_{i,j} + \sum_{q=1}^M (\delta_{qm} \times \beta_{1,q} \times t_{i,j}) + b_{1,i} \times t_{i,j} + \epsilon \quad (6)$$

where $Y_{i,j,m}$ is the response of the i^{th} individual, at the j^{th} time point of the m^{th} treatment group, $\beta_{0,0}$ and $\beta_{1,0}$ are the fixed effect terms for the control group (intercept and slope, respectively), M is the total number of treatment groups, δ_{qm} is the Kronecker delta ($\delta_{qm} = 0$ if $q \neq m$, $\delta_{qm} = 1$ if $q = m$), $\beta_{1,q}$ is the fixed effect term (slope) for the treatment groups, and $b_{1,i}$ is the individual random effects term (slope) of the i^{th} subject, and ϵ is the observation error. The comparison between the control group and the treatment groups was facilitated by separating the fixed effects into different groups, with the control group as the reference.

For the control group, this equation reduces to $Y_{i,j,0} = \beta_{0,0} + \beta_{1,0} \times t_{i,j} + b_{1,i} \times t_{i,j} + \epsilon$. For m^{th} treatment group, this reduces to $Y_{i,j,m} = \beta_{0,0} + (\beta_{1,0} + \beta_{1,m}) \times t_{i,j} + b_{1,i} \times t_{i,j} + \epsilon$. To achieve approximate normality of the response variable $Y_{i,j,m}$, measured quantities of interest (i.e., relative tumor area or relative blood flow) were log-transformed and assigned as $Y_{i,j,m}$. Note that there is an intercept term only in the fixed effect of the reference group, since our variable of interest (rTA and rBF) starts from 1 at Day 0, thus resulting in no intercept in random effects. Equation 6 is further formulated such that the $\beta_{1,m}$ term is a direct comparison between the slopes of the control and treatment group m , and the significance of treatment m is readily available from the p -value of the regression coefficient itself. A Wald test is then utilized to test the null hypotheses that $\beta_{1,m} = 0$. The regression parameters are considered statistically different from those of the control group if $p < 0.05/M_c$, where M_c is the total number of comparisons within each comparison cohort. This significance level was chosen in accordance with Bonferroni correction for multiple comparisons. For example, for the cohort of treatment groups involving doxorubicin and/or cyclophosphamide, responses from 4 different groups were compared with those from the control group. Therefore, $\beta_{1,m}$ with $p < 0.0125$ is deemed to be significantly different from the slope of control group (i.e., $\beta_{1,0}$). Similarly, $p < 0.025$ is deemed statistically significant for the cohort of treatment groups involving different doses of paclitaxel since $M_c = 2$ in this case.

To demonstrate the correlation between blood flow and tumor response estimated by tumor area, a linear regression was performed by assigning group-averaged rBF for the horizontal axis and group-averaged relative tumor area rTA for the vertical axis at a given time point for the control and doxorubicin and/or cyclophosphamide cohort (i.e., treatment group 1-4).

Lastly, a receiver operating characteristic (ROC) curve was constructed to assess the feasibility of using blood flow at early time points to distinguish between treated and untreated mice. First, a treatment group of interest and a control group were pooled together. The predicted positive response was defined as rBF above the threshold (especially for cyclophosphamide-based treatments), and vice versa for predicted negative response. Actual positive and negative response was defined as belonging to the treatment group and the untreated control group, respectively. Then the sensitivity (true positive rate) was calculated by taking a ratio between the number of treated mice showing predicted positive response (i.e., true positive) and the number of all treated mice. Sensitivity here is the measure of the ability to correctly identify individual mice that belong to the treated group. The false positive rate (equivalent to $1 - \text{specificity}$) was calculated as the ratio between the number of control mice with predicted positive response and the number of all mice in the control group. Then, the area under the curve (AUC) was calculated as a measure of discrimination between treated and untreated mice to the specific treatment.

4. Results

4.1. Baseline tumor area and blood flow

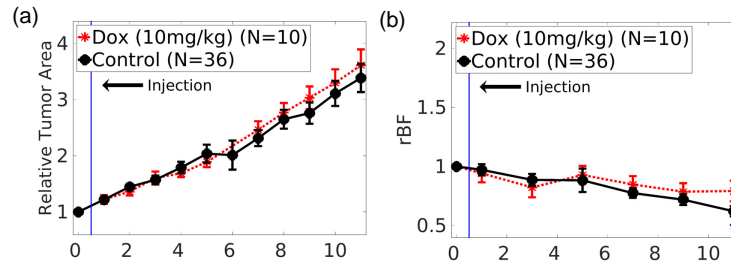
Due to the inter-subject variation in the tumor growth rate, the tumor area at the baseline measurements for individual mice were not uniform. In fact, both tumor area and BFI of 125 mice had a unimodal distribution with positive skew, which approximated to a normal distribution after a log transformation. The 95% confidence intervals for tumor area and BFI were $29.0 - 34.3 \text{ mm}^2$ and $0.99 \times 10^{-8} - 1.11 \times 10^{-8} \text{ cm}^2/\text{s}$, respectively. In order to normalize the intersubject variation, the ratios between subsequent time points and the baseline time point for tumor area and blood flow index were quantified.

4.2. Longitudinal blood flow and tumor size trends under different chemotherapeutic drugs

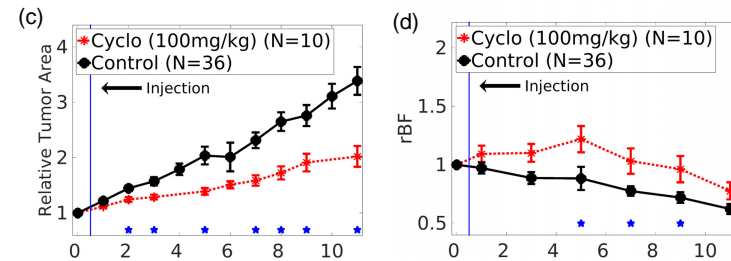
Figure 5 shows group-averaged longitudinal changes of relative tumor area and relative blood flow after a single dose of doxorubicin and/or cyclophosphamide. For clarity of presentation, the group-averaged mean value of either relative tumor area or rBF at each time point are presented for the control group (filled black circle, solid line) and for one treatment group (red asterisk, dotted line) per figure. The error bar in the figure is the standard error of the mean, reflecting the inter-subject variability. The relative tumor area and rBF trend of the group treated with 10 mg/kg of doxorubicin ($N=10$) was not different from those of control group ($N=36$) as seen in Fig. 5(a) and 5(b). For almost every time point, there was no statistically significant difference between control and doxorubicin-only groups in terms of relative tumor area and rBF when student's t-test or Wilcoxon rank-sum test was used. On the other hand, the treatment group with 100 mg/kg cyclophosphamide ($N=10$) showed delayed tumor growth and higher blood flow than the control group (Fig. 5(c) and 5(d)). The relative tumor area difference between the 100 mg/kg cyclophosphamide group and the control group became significant as soon as day 2 and rBF differences were significant on days 5, 7, and 9.

Although doxorubicin alone did not result in tumor growth delay, the combination of doxorubicin and cyclophosphamide ($N=25$) resulted in a more dramatic tumor delay and higher blood flow being sustained even more than 7 days after injection (Fig. 5(e) and 5(f)). In Fig. 5(g) and 5(h), delayed tumor growth and elevated blood flow similar to those with AC treatment were

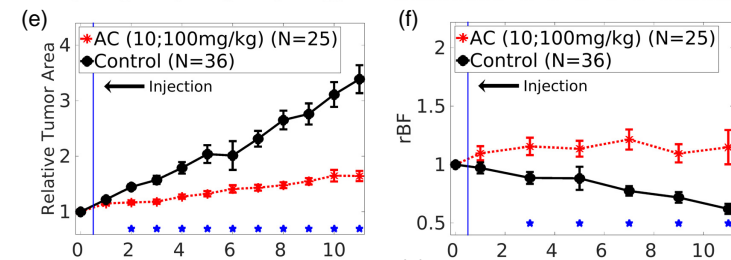
Treatment 1:
Doxorubicin
(10 mg/kg)



Treatment 2:
Cyclophosphamide
(100 mg/kg)



Treatment 3:
Doxorubicin +
Cyclophosphamide
(10; 100 mg/kg)



Treatment 4:
Cyclophosphamide
(200 mg/kg)

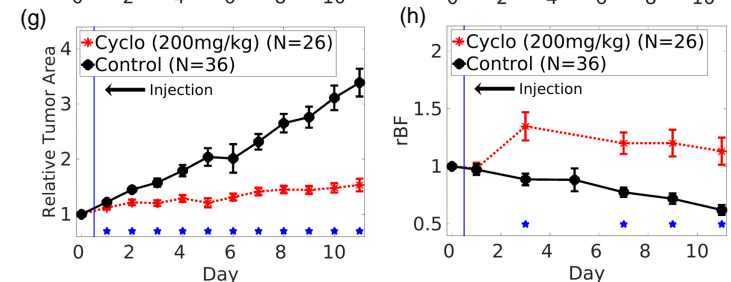


Fig. 5. Group-averaged temporal changes in relative tumor area, rTA (left column) and relative blood flow, rBF (right column) are compared between the control group (filled black circle, solid line) and the treatment group (red star, dotted line). N refers to the number of animals per group. Error bars are derived from the standard error of the mean of each group at each measurement time point. Blue vertical line indicates the time when treatment drug or control vehicle was injected. Blue star indicates statistically significant difference between each treatment and control group based on two-sample test ($p < 0.05$).

observed for the group that received 200 mg/kg cyclophosphamide ($N=26$), which was double the dose compared to treatment 2. In these two treatment groups, relative tumor area difference between the treatment and the control group became significant as soon as day 2 and rBF starting day 3.

The group-averaged longitudinal trends of paclitaxel at different doses are presented in Fig. 6. As seen in Fig. 6(a) and 6(b), relative tumor area and rBF trend of the group treated with 40 mg/kg of paclitaxel ($N=8$) was not different from those of control group ($N=36$). The group

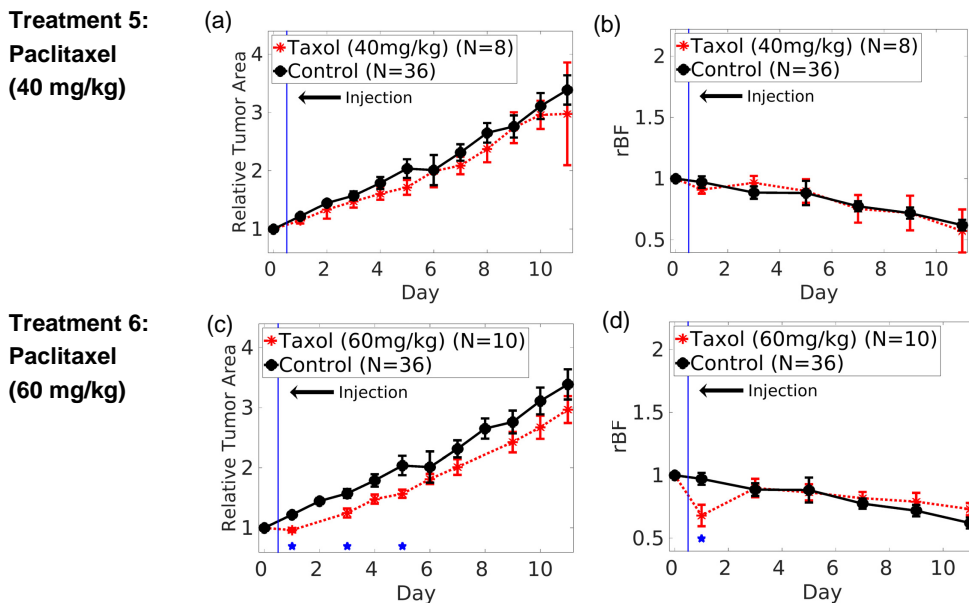


Fig. 6. Group-averaged temporal changes in relative tumor area, rTA (left column) and relative blood flow, rBF (right column) are compared between the control group (filled black circle, solid line) and the treatment group (red star, dotted line). Top and bottom figures are from the group with 40 mg/kg paclitaxel (Taxol) and from the group with 60 mg/kg paclitaxel treatment, respectively. N refers to the number of animals per group. Error bars are derived from the standard error of the mean of each group at each measurement time point. Blue vertical line indicates the time when treatment drug or control vehicle was injected. Blue star indicates statistically significant difference between each treatment and control group based on two-sample test ($p < 0.05$).

treated with 60 mg/kg of paclitaxel exhibited reduction of relative tumor area on day 1, which persisted in later days (Fig. 6(c)). However, the slope of relative tumor area growth after day 3 was the same as that of the control group. The relative blood flow of the 60 mg/kg paclitaxel group decreased drastically on day 1 compared to that of control group, but was similar in other time points (Fig. 6(d)). In terms of time points, there was no statistically significant difference between control and the lower-dose paclitaxel group, whereas the higher-dose paclitaxel group showed significant differences on day 1 after the treatment in both relative tumor area and rBF .

4.3. Statistical difference between treatment group and control group based on linear mixed effects model

Table 2 summarizes the results from the linear mixed effects model. Note that treatment groups are further divided into two different cohorts: one cohort involving either doxorubicin and/or cyclophosphamide (group 1 - 4) and the other cohort with paclitaxel (group 5 - 6). In particular, p -values associated with the slope difference between the treatment and the control group ($\beta_{1,m}$) for relative tumor area and rBF are presented. For the first cohort (group 1 - 4), statistically significant p -value is 0.0125 after Bonferroni correction. Based on this p -value, the doxorubicin-only group (group 1) was not different from the control group, whereas the combination AC group (group 3) and the cyclophosphamide 200 mg/kg group (group 4) were significantly different from the control group in both relative tumor area and rBF . The cyclophosphamide 100 mg/kg group (group 2) exhibited intermediate responses in that relative tumor area was

Table 2. Linear mixed effects model analysis for relative tumor area and relative blood flow of different treatment regimens. p -values for $\beta_{1,m}$ with respect to the control group are presented. * indicates the statistical significance based on Bonferroni correction for multiple comparisons. AC: Adriamycin and cyclophosphamide.

Treatment Group	relative tumor area	relative blood flow
Group 1 (doxorubicin)	0.35	0.46
Group 2 (cyclophosphamide 100 mg/kg)	< 0.0001*	0.034
Group 3 (AC)	< 0.0001*	< 0.0001*
Group 4 (cyclophosphamide 200 mg/kg)	< 0.0001*	< 0.0001*
Group 5 (paclitaxel 40 mg/kg)	0.63	0.57
Group 6 (paclitaxel 60 mg/kg)	0.17	0.11

significantly different from the control group, but rBF , albeit with a relatively low p -value, did not reach the statistical significance after Bonferroni correction.

On the other hand, the treatment cohorts involving paclitaxel did not demonstrate significant difference from the control group in both rTA and rBF , with high p -values (Table 2). The high p -value may be due to similarities in the slope between paclitaxel-based treatments and the control group, although there seems to be an interesting transient change at day 1 for group 6.

4.4. Correlation between blood flow and tumor size changes in response to chemotherapy

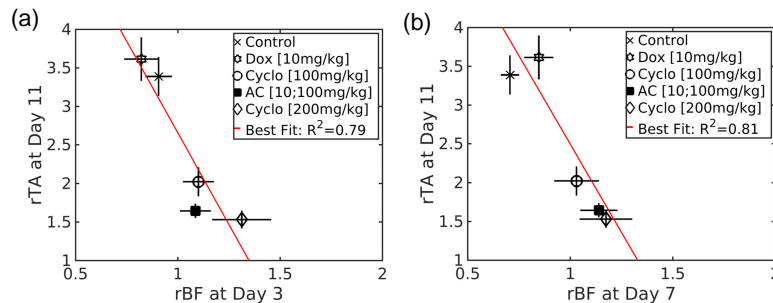


Fig. 7. Correlation between treatment outcome (rTA at Day 11) and rBF at (a) Day 3 or (b) Day 7.

Figure 5 suggests the existence of correlation between the blood flow and the tumor size responses to effective treatments. Clear linear relationships between group-averaged blood flow changes at early time points (day 3 or 7) and group-averaged tumor area change at day 11 (i.e., treatment outcome) are presented in Fig. 7 for the treatment cohort involving doxorubicin and/or cyclophosphamide. Both Fig. 7(a) and 7(b) show high rTA and low rBF for the control and the ineffective treatment (i.e., doxorubicin-only), and low rTA and high rBF for effective treatments involving cyclophosphamide. The Pearson's correlation coefficients were -0.92 (p -value: 0.028) for day 3 and -0.91 ($p < 0.0001$) for day 7, showing relatively strong correlation. Note that we chose to quantify the correlation between rBF at early time points and rTA at day 11 to simulate the clinical situation. Unlike in the animal model, frequent clinical assessment of accurate tumor size during neoadjuvant chemotherapy is difficult due to fibrosis (X-ray mammography or ultrasound) [56–59] or high cost (MRI or PET). Thus, it is reasonable to assume that tumor size information may be available at limited time points (i.e., pre- and post-therapy) from other imaging modalities such as MRI, whereas blood flow can be accessed

frequently through non-invasive diffuse correlation measurements.

4.5. Blood flow changes at early time point as the predictor of responses to chemotherapy

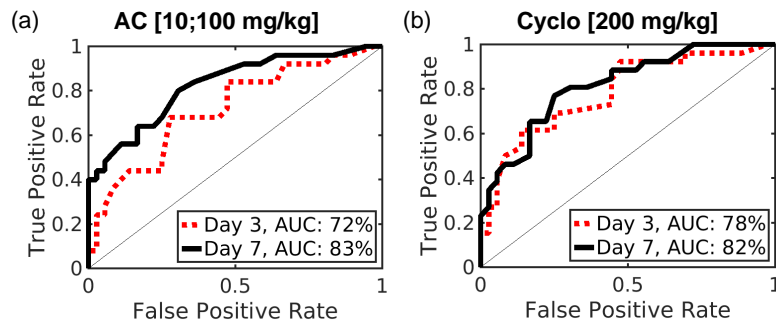


Fig. 8. (a) ROC curve for distinguishing group with AC combination therapy and control group based on rBF at day 3 and 7. (b) ROC curve for distinguishing group with cyclophosphamide 200 mg/kg and control group based on rBF at day 3 and 7.

To determine whether rBF at early time points (e.g., day 3 or 7) can differentiate treated mice from untreated mice on an individual basis, the ROC curves were constructed. Day 5 was not considered due to lack of measurements for the cyclophosphamide 200 mg/kg group. Based on the assessment of linear mixed effects model analysis, the AC combination therapy group (group 3) and higher-dose cyclophosphamide group (group 4) were selected for generation of the ROC curves (Fig. 8). AUC of day 7 was better than day 3 for both treatments, but these AUCs were in similar range (0.72 to 0.83).

5. Discussion

5.1. Significance

In this study, the effects of chemotherapeutic agents on breast cancer blood flow were systematically quantified using longitudinal *in vivo* measurements on a mouse model with diffuse correlation spectroscopy. These measurements demonstrated that the changes in relative blood flow correlated strongly with the treatment efficacy determined by the changes in the relative tumor area.

Even though there have been several longitudinal therapy monitoring studies on animal cancer models with diffuse optical spectroscopy [51,60] and/or diffuse correlation spectroscopy [61,62], this study has several unique and noteworthy aspects in the study design, data analysis method, and findings. First, the tumor model based on orthotopically implanted syngeneic tumors was chosen since it is regarded to be more predictive of responses than ectopic tumors [63]. The mammary fat-pad provides the natural microenvironment for syngeneic tumors. In addition, 4T1 mammary carcinoma grows quickly due to its aggressiveness and shares similarities with human mammary carcinoma especially in terms of metastasis [32]. Second, to improve the quantification of blood flow during the scab formation accompanied with the growth of aggressive breast cancer, we developed a DCS fitting algorithm that adapts either one or two-layer geometry depending on the shape of the correlation function. Here, we combined the approach to fit DCS measurements from multiple source-detector separations [50] and the approach based on the two-layer geometry [46, 64], thereby increasing fitting stability and reducing the discrepancy between measurement and the over-simplified analytical model. Third, six different treatment schemes were investigated to identify the effect of individual drugs, dose

increases and the combination of two drugs as used in the clinic on blood flow. Many aspects of these treatment schemes were designed to reflect characteristics of clinical practice as best as we can within the limitations of the animal model. For example, three commonly used conventional chemotherapeutic drugs for breast cancer were chosen for the study. Their doses for mice were determined with regards to the clinically equivalent doses and the limitation imposed by LD_{50} . For combination therapy, the ratio between doxorubicin and cyclophosphamide was kept the same as that used in the clinic. Lastly, various statistical analysis methods were employed to shed light on clinically motivated questions. A linear mixed effects model was utilized to determine whether longitudinal trends of the relative tumor area or the relative blood flow are statistically different between a certain treatment group and the control group. The ROC curve was generated to test whether the blood flow changes detected at early time points could potentially predict individual response to treatments.

5.2. Physiological observations

Multiple factors such as the tumor type, stage, and microenvironment may affect the hemodynamic changes induced by cancer therapy. Diffuse correlation spectroscopy is a versatile technique that can provide frequent longitudinal measurements of blood flow responses to different cancer therapies in both clinical and preclinical settings. For this particular murine breast cancer model, rBF decreased gradually while the tumor size increased dramatically over 2 weeks in the control group. This decrease in rBF may be due to blood vessel compression caused by growth-induced solid stress [65, 66]. Note that optical measurements were initiated after the tumor reached around 6 mm diameter (around 14 days after tumor inoculation). Two treatment groups showed extremely similar longitudinal trends in relative tumor area and rBF compared to the control group: the group treated with 10 mg/kg of doxorubicin (Group 1) and with 40 mg/kg of paclitaxel (Group 5). Both treatments were administered at a dose less than the clinically equivalent dose. However, mice still exhibited physical symptoms associated with doxorubicin (e.g., weight loss, diarrhea). The high blood vessel compression within the tumor may have hindered the effective delivery of doxorubicin to the tumor. This lack of tumor size difference between the control and the treatment group with 10 mg/kg doxorubicin in the 4T1 tumor model was also observed by Vishwanath *et al.* [51]. Statistically significant difference in blood oxygen saturation between the control and the treatment group was notable at day 10 after doxorubicin administration. In our study, a slight increase of rBF in the doxorubicin group compared to the control group was noted at day 11 after drug administration.

The groups that received treatment regimens involving cyclophosphamide (Group 2-4) exhibited a significant delay in tumor growth compared to the control group, demonstrating the effectiveness of cyclophosphamide-based treatments for the 4T1 tumor model. In parallel, these groups showed prolonged blood flow elevation over time, when compared with the blood flow of the control group. This elevation may be attributed partly to relief of solid stress through tumor growth delay and transient blood vessel renormalization observed in various anti-angiogenic treatments [67].

The combination therapy showed greater effect on tumor size delay and blood flow changes than the monotherapy with cyclophosphamide, despite the fact that the monotherapy with doxorubicin did not exhibit any effect. This synergistic enhancement may be due to the blood flow enhancement from cyclophosphamide leading to better delivery of doxorubicin into the tumor. In the future, we plan to quantify the doxorubicin delivery by detecting fluorescent signals *in vitro* and/or *in vivo*.

Paclitaxel at the 60mg/kg dose also showed a close correlation between the tumor size changes and the blood flow changes. However, its effect was transient, lasting only one day and furthermore exhibited an opposite blood flow change compared to cyclophosphamide-induced blood flow changes. Possible explanations can be found in inefficient delivery of

paclitaxel into the tumor and the anti-angiogenic effect of paclitaxel at low dosages. Although the polyethoxylated castor oil was utilized to improve delivery of water-insoluble paclitaxel, this formulation was known to increase blood vessel viscosity [68] and cause difficulties in delivery. For 4T1 tumors at an advanced stage as utilized in this experiment, the amount of paclitaxel within the tumor may be low enough to induce an anti-angiogenic effect (i.e., killing of endothelial cells) rather than an anti-cancer effect (i.e., killing of cancer cells). The apoptosis of endothelial cells from low dose paclitaxel [42,69] may be the reason for acute size and blood flow decrease. Alternatively, reactive oxygen species generated by paclitaxel [70] may be the cause of transient vasoconstriction.

5.3. Measurement repeatability and the effect of various assumptions in layer models

In this study, thirty consecutive DCS measurements were acquired at the center of the tumor, and three sets of such measurements were performed by lifting the probe up and down. The purpose of the latter measurements was to account for potential variation due to contact-induced pressure on the tumor. The average coefficient of variation (i.e., ratio of the standard deviation to the mean BFI) due to temporal fluctuations from 30 consecutive measurements and placement repeatability from 3 sets was 7% and 10%, respectively. Note that these variations were reduced in our measurements by taking the mean value of several measurements. The spatial heterogeneity of BFI at the center of the tumor was around 8% with probe displacement of 1 - 2 mm.

For the data analysis based on the layer models, several assumptions were made in terms of initial BFI s and optical properties of different layers. The tumor optical properties were assigned as $\mu_{a,2} = 0.1 \text{ cm}^{-1}$ and $\mu'_{s,2} = 8 \text{ cm}^{-1}$ based on optical properties averaged from tumor data available from References [51–53]. Due to the lack of data in the literature, the scab optical properties ($\mu_{a,1}$ and $\mu'_{s,1}$) were assumed to be the same as the tumor properties for computational simplicity. To investigate their effects on the tumor BFI , representative *in vivo* datasets were re-analyzed by varying parameters of interest within the physiological range.

First, initially assumed BFI_1 and BFI_2 were varied in the first part of the two-step fitting process. The variations in the initial values of BFI_1 (1.0×10^{-11} to $1.0 \times 10^{-9} \text{ cm}^2/\text{s}$) and BFI_2 (0.5×10^{-9} to $2.0 \times 10^{-8} \text{ cm}^2/\text{s}$) did not change L and the final extracted tumor blood flow (BFI_2) significantly (i.e., less than 3%).

Second, the effect of μ_a or μ'_s of the scab layer (i.e., layer 1) was investigated by varying μ_a from 0.1 to 0.3 cm^{-1} or μ'_s from 8 to 20 cm^{-1} , respectively. A wide range of optical properties was utilized since the scab optical properties were not available in the literature. μ_a and μ'_s variations resulted in 7% and 10% variation in BFI_2 . These results indicate that BFI_2 is not affected greatly with the optical property variations in the top layer.

Next, the effect of μ_a or μ'_s of the tumor (i.e., layer 2) was investigated based on variations observed in animal studies monitoring cancer treatments [51,71]. According to the longitudinal study comparing doxorubicin-treated and untreated control groups [51], total hemoglobin concentration and average μ'_s were not significantly different between two groups although blood oxygen saturation was. Interestingly, total hemoglobin concentration increased 1.5 times the baseline value and average μ'_s from 8 to 14 cm^{-1} after one week post-treatment. The results from another group [71] did not show an increasing trend of μ'_s , but rather a temporal fluctuation within $\Delta\mu'_s = 2 \text{ cm}^{-1}$ with no significant difference between treated and untreated control groups. For the variation of μ_a of the second layer from 0.1 to 0.15 cm^{-1} , BFI_2 varied from 8 - 10%. For the variation of μ'_s of the second layer from 8 to 12 cm^{-1} , BFI_2 varied from 33 - 50%. The effect of μ'_s of the second layer in the quantification of BFI_2 was the greatest among the assumed parameters thus considered.

However, rBF did not change if the assumed optical properties were varied but held constant over time. Even when we incorporated the increasing temporal trend of μ'_s [51] which resulted

in rBF value changes, the difference between rBF of treated groups and the control group was preserved. In other words, the difference between rBF presented in Fig. 5 is likely to be genuine and not originated from errors in the optical property assumptions.

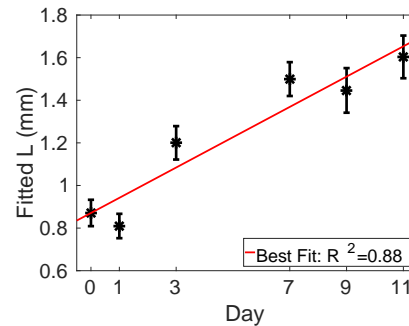


Fig. 9. Group-averaged temporal changes in L from mice in the control group which yielded two-layer model fit. Error bars are derived from the standard error of the mean at each time point.

Note that the first layer thickness L was not varied explicitly, since the two-step fitting process was designed to overcome the sensitivity of the two-layer model on L . Figure 9 shows the longitudinal trend of averaged fitted L for control mice that followed the two-layer model fit, in line with the observation of scab size increase with time. In most cases, once the switch between one-layer model and two-layer model occurred, data followed the two-layer model fit in the following days. Furthermore, the fitted L was positively correlated with the scab thickness estimated from cross-sectional photos from a subset of tumors harvested on day 11. However, the fitted L modestly overestimated the scab thickness which may be due to its sensitivity to the intermediate layer undergoing transition from the tumor to the scab. Since the transitional state may produce a two-layer model-like signal even before the scab becomes visible, the hybrid algorithm was devised to determine the choice of models instead of relying on the visual observation. In the future, quantitative immunohistological analysis on the extent of scab at different time points could increase the fidelity of the layer model approach.

5.4. Limitations and future studies

While relatively strong correlation between early blood flow changes and final tumor size changes was observed for effective treatments, the variations in individual responses were present, affecting the ROC curve. This may be due to potential shifts in the probed region of tumor due to non-uniform growth, limitations of the layer model approach to address spatially heterogeneous formation of scabs, utilization of only a point measurement not accounting for full heterogeneity of the tumor, and assuming constant optical properties throughout the monitoring period. In addition, the observed blood flow changes without treatment (i.e., gradual decrease over time) were opposite to the clinically observed blood flow progression (i.e., increase over time for non-responding tumors). The stage difference between the 4T1 model measured in this experiment (metastasis) [32] and human breast cancers measured in the clinic (mostly before metastasis) would be the most likely cause of the discrepancy in temporal blood flow patterns. For this particular measurement, tumors larger than 6 mm in diameter were measured to ensure contact for measurements at a source-detector separation of 3.94 mm. This limitation resulted in the lack of blood flow information during the tumor growth prior to treatment. To address these limitations, a non-contact scanning diffuse correlation tomography system [72,73] will be adapted for animal cancer monitoring. This will enable measurements of tumors at any time during their development and provide reliable three-dimensional blood flow

imaging with spatially dense datasets from the scanning system. Diffuse optical tomography will be added to the system to provide temporal changes in absorption and scattering coefficients for individual mice. These coefficients will be employed to improve the blood flow accuracy as well as to quantify total hemoglobin concentration and blood oxygen saturation.

6. Conclusion

In this work, we have characterized the longitudinal changes in tumor area and tumor blood flow under various chemotherapy regimens using a 4T1 murine breast cancer model. Relative tumor blood flow was quantified using a layer-model based algorithm, utilizing DCS measurements from multiple source-detector separations simultaneously. The differences between effective and ineffective treatment groups were identified by comparison with the control group using a linear mixed effects model. For treatments involving cyclophosphamide and doxorubicin, relative blood flow changes were inversely correlated with relative tumor area changes. In addition, relative blood flow changes as early as 3 days after cyclophosphamide based treatments exhibited relatively high AUC for distinguishing treated mice from untreated mice. On the other hand, paclitaxel based treatments exhibited a transient blood flow decrease at 1 day after injection which corresponded to tumor area decrease. While the blood flow changes at the early time point correlate well with the tumor size changes, the blood flow response characteristics differ depending on the types of therapeutic drugs as well as the physiology of the tumor model. Diffuse correlation spectroscopy provides means to study these different blood flow characteristics of cancer treatments in animal models. This is the first step towards building a predictive model for effectiveness of breast cancer treatment based on blood flow.

Funding

National Institute of Health (NIH) (K99/R00-CA126187); Fundació Cellex Barcelona; “Severo Ochoa” Programme (SEV-2015-0522); the Obra social “la Caixa” Foundation (LlumMedBcn); Department of Defense (DOD)(BCRP W81XWH-15-1-0040).

Acknowledgements

We thank Hyun Jin Kim for assisting with the construction of the diffuse correlation spectroscopy instrument and Rejune Choe for illustrations. Portions of this work were presented at the OSA Biomedical Optics Conference and Exhibition (BIOMED) meeting in 2016, paper number: CTu4A.4.